Transparent Semiconductor-Superconductor Interface and Induced Gap in an Epitaxial Heterostructure Josephson Junction

Kjaergaard, M.; Suominen, H. J.; Nowak, M.P.; Akhmerov, A. R.; Shabani, J.; Palmstrøm, C. J.; Nichele, F.; Marcus, C.M.

DOI
10.1103/PhysRevApplied.7.034029

Publication date
2017

Document Version
Final published version

Published in
Physical Review Applied

Transparent Semiconductor-Superconductor Interface and Induced Gap in an Epitaxial Heterostructure Josephson Junction

M. Kjaergaard,[1] H. J. Suominen,[1] M. P. Nowak,[2,3,4] A. R. Akhmerov,[2] J. Shabani,[5,*] C. J. Palmstrøm,[5] F. Nichele,[1] and C. M. Marcus[1]

[1]*Center for Quantum Devices and Station Q Copenhagen, Niels Bohr Institute, University of Copenhagen, Universitetsparken 5, 2100 Copenhagen, Denmark*

[2]*Kavli Institute of Nanoscience, Delft University of Technology, P.O. Box 4056, 2600 GA Delft, The Netherlands*

[3]*QuTech, Delft University of Technology, P.O. Box 4056, 2600 GA Delft, The Netherlands*

[4]*AGH University of Science and Technology, Faculty of Physics and Applied Computer Science, al. Mickiewicza 30, 30-059 Kraków, Poland*

[5]*California NanoSystems Institute, University of California, Santa Barbara, California 93106, USA*

(Received 14 July 2016; revised manuscript received 10 January 2017; published 28 March 2017)

Measurement of multiple Andreev Reflection (MAR) in a Josephson junction made from an InAs quantum well heterostructure with epitaxial aluminum is used to quantify a highly transparent effective semiconductor-superconductor interface with near-unity transmission. The observed temperature dependence of MAR does not follow a conventional BCS form but instead agrees with a model in which the density of states in the quantum well acquires an effective induced gap, in our case, 180 μeV, close to that of the epitaxial superconductor, indicating an intimate contact between Al and the InAs heterostructure. The carrier density dependence of MAR is investigated using a depletion gate revealing the subband structure of the semiconductor quantum well, consistent with magnetotransport experiments of the bare InAs performed on the same wafer.

DOI: 10.1103/PhysRevApplied.7.034029

I. INTRODUCTION

The coupling of a semiconducting material with a superconductor allows for the realization of a hybrid system where certain properties of the superconductor can be harnessed in conjunction with the tunability afforded by semiconducting materials. A dramatically increased interest in such hybrid materials stems from the recent proposals to realize hybrid topological materials for quantum-information processing [1–3], as well as the successful demonstration of similar hybrid materials deployed in the setting of superconducting qubits [4,5].

From another perspective, many ballistic and mesoscopic transport effects are expected in semiconductor-superconductor hybrids [6,7] but have not been investigated due to lack of an appropriate material system. In particular, hybrid systems consisting of a superconducting metal in contact with a two-dimensional electron gas (2DEG) were widely explored in previous decades [8–11], but material difficulties hampered progress [11–14].

For all these applications, the quality of the superconductor-semiconductor interface, which controls how superconducting properties are imparted on the semiconductor, is of critical importance [15–17]. In semiconductor nanowires, the difficulty of creating strong uniform coupling to a superconductor was recently resolved by growing the superconductor material *in situ* by molecular beam epitaxy [18]. A hard superconducting gap measured by tunneling into the wire end indicated an intimate coupling between materials [19].

For the purposes of moving to larger integrated devices using hybrid materials for topological (or superconducting) quantum-information processing, a two-dimensional platform, which is amenable to top-down fabrication, provides an alternative and scalable path forward. In particular, state-of-the-art proposals for topological quantum-information processors require (for a single primitive) on the order of approximately six coupled topological regions aligned to quantum dots in a finely tuned manner [20]. Such a device will be dramatically simpler to construct starting from a 2D platform, as opposed to alignment of individual nanowires. Similarly, for superconducting qubits, where scalability is one of the main research directions of the field [21], the hybrid nanowire-based approach will benefit from circumventing the need for precise placement of individual nanowires by instead using Josephson junctions embedded in a 2D geometry as the nonlinear element.

A first step towards such 2DEG-based hybrid materials was recently reported, where *in situ* growth of Al was applied to InAs 2DEGs [22]. This system also exhibits a hard superconducting gap in tunnel spectroscopy [23], similar to the result for nanowires. Here we expand in detail

*Present address: City College, City University of New York, New York, NY, USA.

the results on 2DEG-based hybrid materials by studying the properties of a planar Josephson junction amenable to both the pursuit of topological materials [24,25] and gateable superconducting qubits formed using top-down processing of InAs 2DEG with *in situ* Al grown.

II. THE JOSEPHSON JUNCTION IN A QUANTUM-WELL HETEROSTRUCTURE

We report multiple Andreev reflections (MARs) in a gateable Josephson junction formed from an InAs 2DEG epitaxial Al heterostructure. We observe a temperature dependence of the MAR peak positions that differs from expectations for a conventional BCS-like gap, but it is consistent with an induced gap in the InAs under the Al [16,17,26,27]. The appearance of an induced gap Δ^* in the local density of states of the semiconductor reflects the finite time a state from the quantum well spends in the superconductor [28]. Comparing MAR data to a quantitative model (described below), we infer an induced gap $\Delta^* = 180$ μeV in the InAs region covered by Al and a transmission through the effective interface formed at the boundary between the covered and uncovered InAs in excess of 97%. These results are consistent with tunnel spectroscopy measurements on the same wafer [23].

The high transparency of our junction is further confirmed by the shape of the MAR features, where we observe *dips* in conductance when the applied voltage is a fraction of the gap, $V = 2\Delta^*/en$. This dip-to-peak transition in conductance is a longstanding prediction for highly transparent junctions [29] also confirmed by our quantitative modeling. To our knowledge, this inversion is often overlooked in the experimental literature, even for junctions considered highly transparent (see, for instance, Refs. [30–32]), leading to erroneous identification of the gap. We discuss the dip-to-peak transition further in Sec. IV below.

Modeling also reveals the existence of two distinct families of MAR resonances at zero top-gate voltage, which we associate with two occupied subbands in the 2DEG. By energizing a top gate on the exposed 2DEG, the resonant features change, becoming consistent with single-subband occupancy. The gate-dependent change from two to one subband is consistent with magnetotransport measurements on a Hall bar with the Al removed, fabricated on the same wafer.

III. DEVICE CHARACTERIZATION

The hybrid heterostructure used in this study is grown by molecular beam epitaxy and consists (from top to bottom) of 10-nm Al, 10-nm $In_{0.81}Ga_{0.19}As$, 7-nm InAs (quantum well), 4-nm $In_{0.81}Ga_{0.19}As$, and an $In_xAl_{1-x}As$ buffer on an InP wafer. We emphasize that the Al layer is grown *in situ* as part of the heterostructure [22]. Density $n = 1.26 \times 10^{12}$ cm^{-2} and mobility $\mu = 15\,600$ cm^2/V s measured in a top-gated Hall bar geometry with the Al removed yield a mean free path

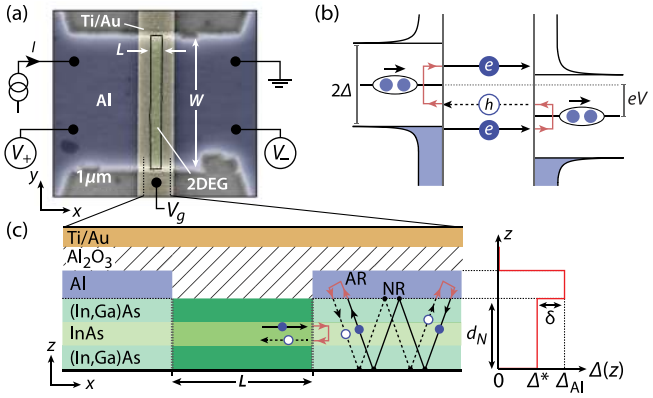

FIG. 1. (a) False-color scanning electron micrograph of the *S*-2DEG-*S* device. (b) Schematic of the second-order MAR process when a voltage $eV < \Delta$ is applied across an ideal superconductor–normal-metal–superconductor (*S*-*N*-*S*) junction. (c) Cross-sectional schematic of the device in (a) (not to scale). Because of processes such as the one sketched in the schematic involving multiple Andreev reflections (ARs) and potentially also normal reflections (NRs), the part of the quantum well covered by Al gains an induced gap Δ^*. Andreev reflections of particles in the uncovered region happen at the vertical *effective* interface indicated by the gray vertical dashed line stemming from the gap Δ^* in the quantum well. Right schematic indicates variation of superconducting gap $\Delta(z)$ in the growth direction for the case of an effective quantum-well thickness much less than the normal-state coherence length $d_N \ll \xi_N$ (see text for details) in the part of the quantum well covered by Al.

$l_e \sim 290$ nm at top-gate voltage $V_g = -2.5$ V. As demonstrated below, at $V_g = 0$ the quantum well has two subbands occupied (see, also, Appendix A).

The wafer is patterned into mesa structures using a standard III-V wet etch. The Al is then patterned using a selective Al etch (Transene D). Next, an unpatterned 40-nm aluminum oxide layer is deposited using atomic layer deposition. Finally, a Ti/Au gate is deposited, patterned to cover the exposed 2DEG. Figure 1(a) shows a false-color scanning electron micrograph of the final device, and Fig. 1(c) shows a schematic cross section through the junction. The exposed 2DEG region has a length $L \simeq 250$ nm and a width $W = 3$ μm. The superconducting gap of the 10-nm-thick Al layer is inferred from the critical temperature ($T_c = 1.56$ K, independently measured in four-terminal measurement) via $\Delta_{\mathrm{Al}} = 1.76 k_B T_c = 237$ μeV. We note that the gap of the Al layer is larger than bulk Al [33], with a T_c consistent with previously reported values [34,35].

All measurements are performed in a dilution refrigerator with base temperature $T \sim 30$ mK using standard dc and lock-in techniques, with current excitation in the range 2.5 to 5 nA.

IV. MULTIPLE ANDREEV REFLECTIONS IN QUANTUM-WELL JOSEPHSON JUNCTIONS

The theoretical approach to this system begins with the Octavio-Blonder-Tinkham-Klapwijk (OBTK) model for

multiple Andreev reflections [36]. As originally formulated, this model assumes a well-defined voltage is dropped across the normal region [green rectangle in Fig. 1(a)], leading to the MAR process sketched in Fig. 1(b). For a planar junction where the 2DEG extends *under* the Al [Fig. 1(c)], the voltage can also drop along the horizontal Al 2DEG interface. In the case of imperfect Al 2DEG transparency, this voltage drop leads to smearing of the resonances arising from MAR [37,38]. The OBTK model was later extended to account for the planar geometry [26] denoted *S-N-c-N-S*, where *c* is the semiconducting region in which the superconducting top layer is removed. The *S-N* electrodes consisting of 2DEG with Al on top are assumed to be disordered and in equilibrium, while the exposed 2DEG region of length L is assumed ballistic. The model yields a renormalized density of states in the 2DEG, with an induced gap $\Delta^* < \Delta_{\mathrm{Al}}$ determined by the quality of the interface between the quantum well and the Al [26].

Figure 2 shows differential conductance (left) and dc voltage (right) as a function of applied dc current for two gate voltages. The inset in Fig. 2(a) shows an enlargement indicating the excess current and critical current for $V_g = 0$ V. The critical current is $I_c = 1.77$ μA yielding an I_cR_n product of 165 μeV, about 70% of the gap of the Al film, and a critical current density $J_c = I_c/W = 0.59$ μA/μm. The excess current reflecting enhanced current through the junction due to Andreev reflection is defined as the $V = 0$ intercept of a linear fit to $V(I)$ taken at $V \gg \Delta_{\mathrm{Al}}/e$ [green dashed line in Fig. 2(a)]. The measured excess current $I_{\mathrm{exc}} = 1.44$ μA corresponds to $I_{\mathrm{exc}}R_n = 140$ μeV [the excess current can be related to the gap via $I_{\mathrm{exc}} = \alpha\Delta/eR_n$, where $\alpha = 8/3$ in the ballistic, fully transparent case [15], and $\alpha = (\pi^2/4–1)$ in the fully diffusive case [39]]. The differential conductance [red curve in Fig. 2(a)] shows a series of peaks and dips as the current is increased. The peak and dip structure is a manifestation of the MAR processes and is expected to follow the series $eV = 2\Delta/n$, with $n = 1, 2, 3, \ldots$ corresponding to the number of Andreev reflections.

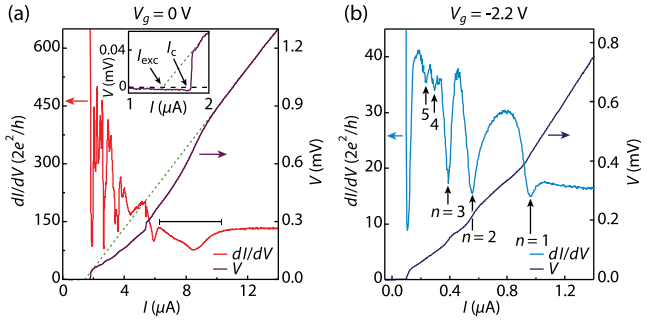

FIG. 2. Differential conductance (left axis) and dc voltage (right axis) at two different gate voltages. In (a), the dashed green line shows linear fit at $eV(I) \gg \Delta_{\mathrm{Al}}$ used to extract the excess current I_{exc} as the intercept with the $V = 0$ mV (as shown in the inset). I_c is the current at which the system switches to a resistive state. The dips highlighted in (b) correspond to multiple Andreev reflections of order *n*.

However, a broad dip in conductance highlighted with black horizontal bar in Fig. 2(a) occurs at energies larger than 2Δ but follows the temperature dependence of I_c and disappears at T_c (cf. Fig. 7 in Appendix B) indicating that the feature has a superconductive origin. Such anomalous resistance features are believed to be associated with the planar Josephson-junction geometry [40,41], where quasiparticles in the 2DEG can undergo several scattering events at the Al interface before ultimately undergoing Andreev reflection and traversing the same path back. On a length scale smaller than the normal-state coherence length $\xi_N = \hbar v_F/k_BT$, this process appears as an Andreev reflection from an *effective* boundary indicated by the gray vertical dashed line in Fig. 1(c). The finite-bias properties of such systems cannot be adequately described by either the *S-N-c-N-S* or OBTK models, and the simple picture in Fig. 1(b) breaks down. With the contacts out of equilibrium, the position of the peaks in Fig. 2(a) cannot be directly related to the superconducting gap. However, by increasing the resistance in the exposed region relative to the horizontal interface, the peaks at finite bias follow a regular series and can be used to extract a value for the induced gap.

In Fig. 2(b), the gate covering the exposed 2DEG region is energized to $V_g = -2.2$ V, substantially depleting the junction, leading to a normal-state resistance $R_n = 740$ Ω. At this gate voltage, the broad conductance dip at energies $eV > 2\Delta_{\mathrm{Al}}$ is absent, and the dc voltages of the first three peaks (indicated with vertical black arrows) are positioned proportional to $1/n$, indicating that the voltage drop now occurs predominantly in the 2DEG region not covered by Al. At this gate voltage, I_cR_n is reduced from the $V_g = 0$ value (full I_cR_n versus V_g is shown in Fig. 8 of Appendix C). As we show below, the *I-V* curves in Fig. 2 are consistent with near-unity transmission through a *S-N-c-N-S* junction.

In highly transparent junctions, the resonances due to MAR appear as dips in the differential conductance, as opposed to the often-used peaks. This subtle point can be appreciated by considering the nature of the current in a Josephson junction at finite voltages. In general, the current is a combination of the number of Andreev reflections n and the transmission τ of the junction. For the nth-order Andreev reflection, the particle traverses the normal region $n+1$ times, and neglecting the energy dependence of Andreev reflection probability, the current depends on transmission as

$$I(V) \sim (n+1)\tau^{n+1}V. \tag{1}$$

For low τ, the current, thus, decreases rapidly for higher-order Andreev reflection processes (i.e., increasing n). In

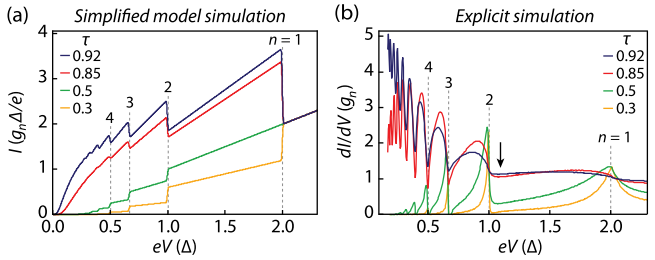

FIG. 3. (a) Current through a *S*-*N*-*S* junction from the simplified model of Eq. (1) in units of $g_n\Delta/e$ (g_n is the normal-state conductance), for several values of transmission through the junction. (b) Conductances of a *S*-*N*-*S* junction calculated using the scattering approach for different values of the transparency τ. The vertical black arrow indicates the position of the conductance dip discussed in detail in Sec. VI.

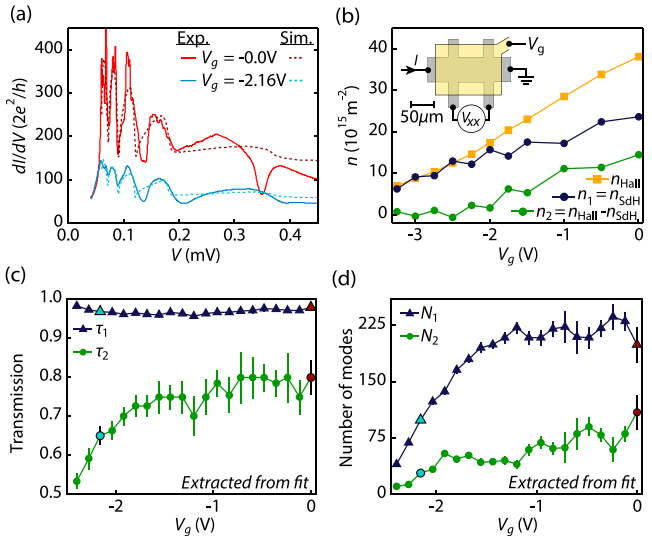

FIG. 4. (a) Conductance as a function of bias voltage at two different gate voltages exhibiting resonances due to MAR. (b) Density in the 2DEG extracted from the Hall slope and power spectrum of Shubnikov–de Haas (SdH) oscillations versus gate voltage (see text for details). (c),(d) Transparency τ_i and number of modes N_i in subband i as a function of top-gate voltage V_g extracted from the MAR data in (a). The red and teal points correspond to the fitting values used for the dashed curves in panel (a).

contrast, for very transparent interfaces, higher-order Andreev reflections will still yield an appreciable contribution to the current. This situation is demonstrated in Fig. 3(a), where we show the current in a *S*-*N*-*S* device calculated according to Eq. (1). For low transparencies, the slope of the I versus V curves *increases* as n decreases, and the current increases at the transition from n to $n-1$ Andreev reflections. As a result, the conductance of opaque junctions forms a staircase pattern that increases in voltage with peaks at the subgap features [cf. the conductance depicted with the orange and green curves in Fig. 3(b) calculated using the model of Ref. [29]]. In contrast, in the transmissive junctions, the current curve exhibits an opposite pattern, which results in a declining staircase pattern in the conductance with the peaks replaced by dips [see the purple curve in Fig. 3(b)]. This effect leads to an overall increase in the conductance *between* values of the voltage corresponding to integer multiples of the gap (i.e., at $V = 2\Delta/en$). Therefore, the vertical arrows in Fig. 2(b) point to local *minima*, not maxima, in conductance to indicate multiples of the gap arising from the relation $V = 2\Delta/en$.

V. ELECTROSTATIC GATE DEPENDENCE

To extract the value of Δ^*, we plot the conductance from Fig. 2 against the dc voltage drop, as shown in Fig. 4(a). The theoretical MAR resonances in Fig. 4(a) are simulated using a generalized scattering matrix approach developed for *S*-*N*-*S* junctions [29,42]. Within the model of an induced gap [26], the *S*-*N*-*c*-*N*-*S* system is interpreted as an effective S^*-*N*-S^* junction, where S^* is the superconducting quantum well covered by Al with a gap Δ^* and a critical temperature identical to that of the parent superconductor. Simulations are performed by calculating the conductance $G^{(\tau)}(V)$ of a single mode with transmission τ from the dc component of the current $I^{(\tau)}(V,t) = \sum_k I_k^{(\tau)} \exp(2ikeVt/\hbar)$. The time-independent Fourier component of I_k is calculated from the wave functions of the quasiparticles accelerated by the voltage V across the junction. In the case of a ballistic junction ($L < l_e$), the backscattering effectively occurs only at the boundary between $S^\star$ and N [vertical gray dashed line in Fig. 1(c)]. The total current through the junction is the sum of currents carried by N modes in M subbands. The resulting conductance through the multimode junction is given by $G(V) = \sum_i^M N_i G^{(\tau_i)}(V)$ where N_i is the number of modes in the ith subband, and τ_i is the transmission of the modes in the ith subband.

A nonlinear least-squares procedure is used to fit simulated $G(V)$ curves to the data in Fig. 4(a), where τ_i, $\Delta^\star$, and N are fitting parameters, and M is predefined (see, also, Ref. [43]). The minimal number of subbands needed to capture the essential features of the data is found to be $M = 2$. For $M > 2$, the optimal fit does not populate the $i > 2$ subbands (i.e., $N_i \sim 0$ for $i > 2$), indicating that the data are well described by two subbands (in Fig. 9 of Appendix D, we show simulations using $M = 1$ and $M = 3$). The result of fitting to the MAR features at two V_g values are shown as dashed curves in Fig. 4(a). At $V_g = 0$, the induced gap is $\Delta^* = 182$ μeV with $N_1 = 199$, $N_2 = 109$, $\tau_1 = 0.98$, and $\tau_2 = 0.8$. When the gate is energized to $V_g = -2.2$ V, the fitting values are $\Delta^* = 180$ μeV, with $N_1 = 100$, $N_2 = 29$, $\tau_1 = 0.97$, and $\tau_2 = 0.65$. The gate-voltage dependence of the fitting parameters τ_i and N_i are shown in Figs. 4(c) and 4(d).

The gap Δ^* extracted from the fitting routine is identical to the one measured in a tunneling experiment on the same wafer [23].

The presence of two transmission species in the optimal fit is attributed to the 2DEG having two occupied subbands. The carrier density in the 2DEG denoted n_{Hall} is measured in a Hall bar geometry via the Hall slope [shown in Fig. 4(b)]. The density from the Hall slope is compared to the density extracted from the periodicity of the Shubnikov–de Haas (SdH) oscillations in an out-of-plane magnetic field. The data in Fig. 4(b) show the density change in the 2DEG as the top gate is energized. The power spectrum of $\rho_{xx}(1/B)$ exhibits a two-peak structure indicating two subbands with different densities in the quantum well at $V_g = 0$ V [44]. The density corresponding to the major peak is denoted n_1, and the difference $n_{\mathrm{Hall}} - n_1$ is denoted n_2. The density in the two subbands changes as the top gate is energized, as shown in Fig. 4(b), similar to N_1 and N_2 extracted from fitting to the MAR features. In particular, the N_2 species becomes depopulated at a gate voltage similar to the depletion of the second subband in the Hall bar [Fig. 4(b)]. The decrease of transmission of the $i = 2$ species in Fig. 4(c) could be due to a breakdown of the ballistic assumption as the second subband is depleted.

Within the 1D Blonder-Tinkham-Klapwijk formalism for a *S*-*N* interface, the transparency is often parametrized using the dimensionless quantity Z related to the transmission via $\tau^{-1} = (1 + Z^2)$ [15]. For the first subband, we extract an average transmission $\bar{\tau}_1 \gtrsim 0.97$ corresponding to a Z parameter of $Z_1 \lesssim 0.18$. This low Z parameter indicates that the effective interface between the uncovered quantum well and the region covered by Al is pristine.

VI. ELUCIDATING THE INDUCED GAP

The distinction between a BCS-like gap Δ_{Al} and an induced gap Δ^* is revealed through the temperature dependence of the superconducting properties. In the case where the effective thickness of the quantum well is much less than the normal-state coherence length $d_N \ll \xi_N$, any position dependence of the gap magnitude in the growth direction in the 2DEG can be neglected, and the temperature dependence of the induced gap depends on Δ_{Al} according to [10,26,45]

$$\Delta^*(T) = \frac{\Delta_{\mathrm{Al}}(T)}{1 + \gamma_B \sqrt{\Delta_{\mathrm{Al}}^2(T) - \Delta^{*2}(T)}/\pi k_B T_c}, \qquad (2)$$

where $\Delta_{\mathrm{Al}}(T)$ is determined self-consistently from BCS theory. The dimensionless parameter γ_B is a measure of the horizontal *S*-*N* interface transparency [black horizontal dashed line in Fig. 1(c)], where $\gamma_B = 0$ corresponds to a perfectly transparent interface [46]. The parameter γ_B represents the discontinuity in the superconducting pair potential and gives rise to the difference between the gap in aluminum Δ_{Al} and the induced gap Δ^* in the 2DEG denoted δ in Fig. 1(c). For the present case, we find $\gamma_B = 0.87$ using $\Delta^* = 180$ μeV and $\Delta_{\mathrm{Al}} = 237$ μeV consistent with a high-quality interface between the quantum well covered by Al and the Al itself.

To elucidate the nature of the induced superconducting gap, we study the temperature dependence of the differential conductance at $V_g = -2.2$ V shown in Fig. 5(a). The position of the second MAR-related dip (denoted p_2) is tracked in Fig. 5(b) as the temperature is increased. The curves in Fig. 5(b) show the solution of Eq. (2) (purple), temperature dependence of a BCS gap $\Delta_{\mathrm{Al}}(T)$ (teal), and a BCS-like gap $\Delta'_{\mathrm{Al}}(T)$ (teal, dashed), where the gap value is rescaled to coincide with the data at $T = 30$ mK. The inadequacy of the temperature dependence of a BCS-like gap (both unscaled and rescaled) to account for the temperature dependence of the peaks is contrasted by the good correspondence between Eq. (2) and our data. The temperature dependence of the first and third dip positions p_1 and p_3 are shown in Fig. 5(c). The curves identified with p_1 and p_3 are found by multiplying $\Delta^*(T)$ by a factor of 2 and 2/3, respectively, corresponding to $n = 1$ and $n = 3$ in the $2/n$ MAR series.

The small deviation between $V(p_2) \sim 0.21$ meV, which one might expect is located at $V = 2\Delta^*/(2e) = \Delta^*/e$, and the gap extracted from the fitting in Sec. V ($\Delta^* \sim 0.18$ meV) can be understood by again appealing to the simulation in Fig. 3(b). There, the black vertical arrow shows the minimal conductance close to the $n = 2$ MAR resonance, which does not coincide exactly with

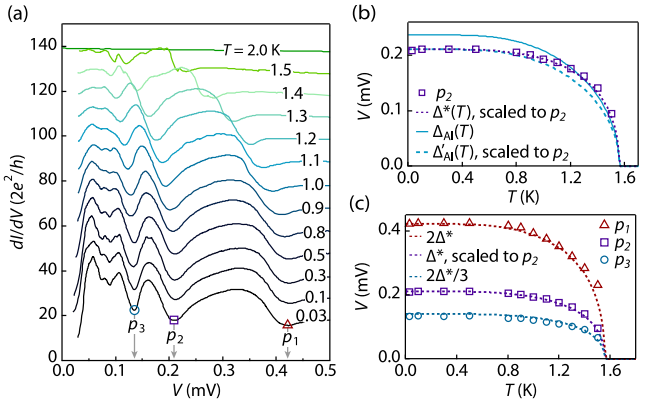

FIG. 5. (a) Temperature dependence of the MAR features at $V_g = -2.2$ V. Traces successively offset by $10 \times 2e^2/h$. (b) Temperature dependence of the dip labeled p_2. Dashed purple line is Eq. (2) scaled to match p_2 at base temperature. The solid teal line is the temperature dependence of a BCS superconducting gap, and the dashed teal line is a rescaling of $\Delta_{\mathrm{Al}}(T)$ to match p_2 at base temperature. (c) Temperature dependence of first, second, and third dip positions with multiples of $\Delta^*(T)$ from (b).

Δ/e. From the simulation, we see that the voltage difference from the resistance maxima at the vertical arrow and the gap is approximately 10%, in good agreement with $V(p_2)$ and Δ^* which differ by approximately 14%. Regardless, the correspondence between the temperature dependence of the MAR features and temperature dependence of the gap is unchanged by this effect, and the excellent agreement also with $n = 1$ and $n = 3$ resonances indicates that the superconducting properties of the junction are well described within the induced gap model.

VII. CONCLUSION AND OUTLOOK

In conclusion, we measure MAR resonances in a Josephson junction in an InAs 2DEG heterostructure, where aluminum is epitaxially matched to the 2DEG. By fitting the conductance of the MAR features, we extract a transmission close to unity through an effective S^*-N-S^* junction, where S^* represents the InAs quantum well covered by the Al. The temperature dependence of the MAR resonances is well described by the theory of an effective induced gap, and we find $\Delta^* = 180\ \mu$eV in the 2DEG region covered by Al, close to the gap of the Al itself, indicating a transparent interface between the two.

The intrinsic flexibility offered by the hybrid system presented here, combined with the quality of the coupling between semi- and superconductor, makes this material a promising candidate for exploring scalable topological and superconducting quantum-information systems. As an example of this platform, we mention that the quality of the 2DEG allows a monotonic suppression of I_c as the top gate is used to deplete (shown in Fig. 8). Such a property is highly desirable within the gatemon superconducting-qubit architecture, where the qubit frequency is determined in part by the value of I_c and is the key control parameter [47]. Finally, we mention that several recent proposals [24,25] show that planar Josepshon junctions, as the type that we demonstrate here, can be tuned into a topological regime with minor adjustments to the device geometry.

ACKNOWLEDGMENTS

We thank Karsten Flensberg for valuable discussions. Research support is provided by Microsoft and the Danish National Research Foundation. C. M. M. acknowledges support from the Villum Foundation. F. N. acknowledges support from a Marie Curie Fellowship (Grant No. 659653). M. P. N. acknowledges support from ERC Synergy Grant. A. A. is supported by an ERC Starting Grant, the Foundation for Fundamental Research on Matter, and the Netherlands Organization for Scientific Research as part of the Frontiers of Nanoscience program.

M. K. and H. J. S. contributed equally to this work.

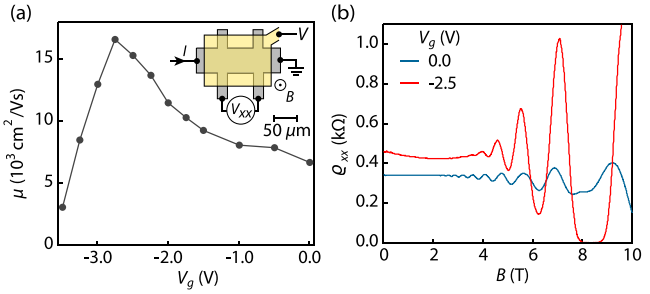

FIG. 6. (a) Mobility of the 2DEG as a function of top-gate voltage measured in a Hall bar. (b) Shubnikov–de Haas oscillations at two values of top-gate voltage in a Hall bar.

APPENDIX A: MOBILITY PEAK AND SUBNIKOV–DE HAAS OSCILLATIONS

In Fig. 6(a), the gate dependence of the 2DEG mobility is shown, measured in the same Hall bar as the data in Fig. 4(b) of the main text. The mobility peak is at $V_g = -2.75$ V, the same gate-voltage value at which $n_2 \approx 0$ [see Fig. 4(b)], consistent with the interpretation of a mobility-limiting second subband being depleted. Two examples of Shubnikov–de Haas oscillations of ρ_{xx} are shown in Fig. 6(b) at $V_g = 0$ V (the two-subband regime) and $V_g = -2.5$ V (the one-subband regime).

APPENDIX B: TEMPERATURE DEPENDENCE OF THE ANOMALOUS RESISTANCE PEAK

Figure 7 shows the evolution of the differential resistance as the temperature is increased at $V_g = 0$ V. The anomalous resistance peak discussed in Fig. 2(a) of the main text (highlighted with horizontal black bar) has identical temperature dependence to other superconducting features of the device. The complementary data at $V_g = -2.2$ V are shown in Fig. 5 and are used for extracting the temperature dependence of the gap.

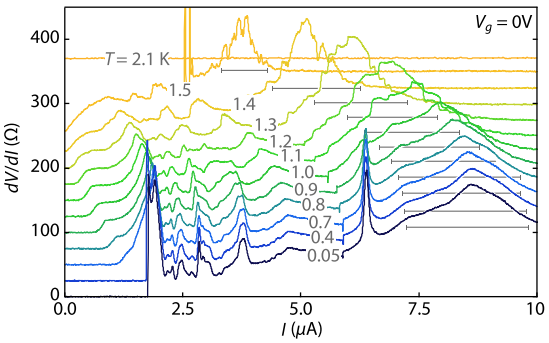

FIG. 7. Temperature dependence of differential resistance at $V_g = 0$ V. Curves successively offset by 25 Ω, except for $T = 0.05$ K. Horizontal bars indicate positions of the anomalous resistance peak.

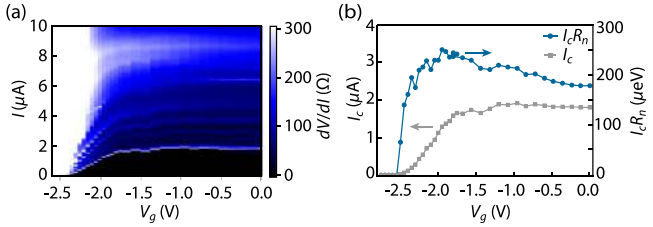

FIG. 8. (a) Differential resistance of the junction as the current I is swept when the gate V_g is energized. (b) The value of I_c and I_cR_n extracted from (a), as a function of gate voltage.

APPENDIX C: GATE DEPENDENCE OF THE SUPERCONDUCTING PROPERTIES OF THE 2DEG

The gate-voltage dependence of the differential resistance of the S-2DEG-S junction is shown in Fig. 8. At $V_g = -2.5$ V, the junction is no longer able to sustain a supercurrent, and the normal-state resistance is $R_n \approx 1.7\,\mathrm{k\Omega}$. The I_cR_n product has only a weak dependence on gate voltage [Fig. 8(b)], with a maximum $I_cR_n \sim 250\ \mu$eV at $V_g = -1.95$ V.

APPENDIX D: SUBBANDS IN THE SIMULATIONS

In the main text, we introduce the simulations used to fit the MAR features in Fig. 4(a). The fit procedure takes as input a fixed number of subbands denoted M, which can have a different number of modes N and transmission τ. At $V_g = 0$ V, we find the optimal subband number is $M = 2$. As shown in Fig. 9, at $M = 1$ the fit is visibly worse, while for $M = 3$ the optimal least-squares fit to the experimental data does not involve any modes in the third subband, i.e., $N_3 = 0$. We note that for $M = 3$ and a specific choice of the initial guess of the parameters, the fitting procedure can distribute modes among all three subbands, creating two subbands that are almost degenerate in transmission probability. When this happens, the fitting errors of N_i and τ_i are

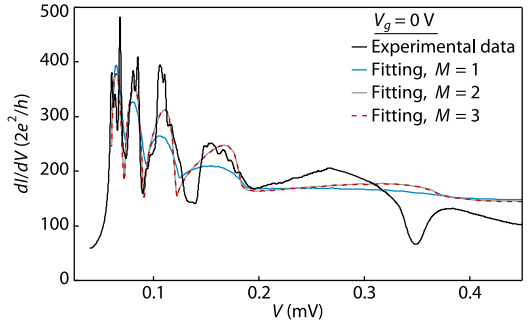

FIG. 9. Fit to experimental data at $V_g = 0$ V (black curve) for several values of the number of occupied subbands M used in the simulation.

TABLE I. Optimal value of N_i, the number of modes in subband i, for different number of subbands M in the simulation. n.a. indicates that a fitting parameter is not applicable.

$M = 1$	$M = 2$	$M = 3$
$N_1 = 299$, $\tau_1 = 0.97$	$N_1 = 199$, $\tau_1 = 0.98$ $N_2 = 109$, $\tau_2 = 0.8$	$N_1 = 185$, $\tau_1 = 0.98$ $N_2 = 123$, $\tau_2 = 0.82$ $N_3 = 0$, $\tau_3 =$ n.a.

larger than the fitted values by several orders of magnitude, and, hence, we disregard such solutions. In Table I, we list the number of modes in the optimal least-squares fit for $M = 1, 2, 3$.

[1] Jason Alicea, Yuval Oreg, Gil Refael, Felix von Oppen, and Matthew P. A. Fisher, Non-Abelian statistics and topological quantum information processing in 1D wire networks, Nat. Phys. **7**, 412 (2011).

[2] Martin Leijnse and Karsten Flensberg, Quantum Information Transfer between Topological and Spin Qubit Systems, Phys. Rev. Lett. **107**, 210502 (2011).

[3] David Aasen, Michael Hell, Ryan V. Mishmash, Andrew Higginbotham, Jeroen Danon, Martin Leijnse, Thomas S. Jespersen, Joshua A. Folk, Charles M. Marcus, Karsten Flensberg, and Jason Alicea, Milestones Toward Majorana-Based Quantum Computing, Phys. Rev. X **6**, 031016 (2016).

[4] T. W. Larsen, K. D. Petersson, F. Kuemmeth, T. S. Jespersen, P. Krogstrup, J. Nygård, and C. M. Marcus, Semiconductor-Nanowire-Based Superconducting Qubit, Phys. Rev. Lett. **115**, 127001 (2015).

[5] G. de Lange, B. van Heck, A. Bruno, D. J. van Woerkom, A. Geresdi, S. R. Plissard, E. P. A. M. Bakkers, A. R. Akhmerov, and L. DiCarlo, Realization of Microwave Quantum Circuits Using Hybrid Superconducting-Semiconducting Nanowire Josephson Elements, Phys. Rev. Lett. **115**, 127002 (2015).

[6] C. W. J. Beenakker, Universal Limit of Critical-Current Fluctuations in Mesoscopic Josephson Junctions, Phys. Rev. Lett. **67**, 3836 (1991).

[7] C. W. J. Beenakker, Quantum transport in semiconductor-superconductor microjunctions, Phys. Rev. B **46**, 12841 (1992).

[8] Hideaki Takayanagi, Jorn Bindslev Hansen, and Junsaku Nitta, Mesoscopic Fluctuations of the Critical Current in a Superconductor–Normal-Conductor–Superconductor, Phys. Rev. Lett. **74**, 166 (1995).

[9] H. Takayanagi, T. Akazaki, and J. Nitta, Observation of Maximum Supercurrent Quantization in a Superconducting Quantum Point Contact, Phys. Rev. Lett. **75**, 3533 (1995).

[10] A. Chrestin, T. Matsuyama, and U. Merkt, Evidence for a proximity-induced energy gap in Nb/InAs/Nb junctions, Phys. Rev. B **55**, 8457 (1997).

[11] T. Bauch, E. Hürfeld, V. Krasnov, P. Delsing, H. Takayanagi, and T. Akazaki, Correlated quantization of supercurrent and conductance in a superconducting quantum point contact, Phys. Rev. B **71**, 174502 (2005).

[12] L. C. Mur, C. Harmans, J. E. Mooij, J. F. Carlin, and A. Rudra, Experimental indication for supercurrents carried by opened transport channels, Phys. Rev. B **54**, R2327 (1996).
[13] F. Giazotto, K. Grove-Rasmussen, R. Fazio, F. Beltram, E. H. Linfield, and D. A. Ritchie, Josephson current in Nb/InAs/Nb highly transmissive ballistic junctions, J. Supercond. **17**, 317 (2004).
[14] M. Amado, A. Fornieri, F. Carillo, G. Biasiol, L. Sorba, V. Pellegrini, and F. Giazotto, Electrostatic tailoring of magnetic interference in quantum point contact ballistic Josephson junctions, Phys. Rev. B **87**, 134506 (2013).
[15] G. E. Blonder, M. Tinkham, and T. Klapwijk, Transition from metallic to tunneling regimes in superconducting microconstrictions: Excess current, charge imbalance, and supercurrent conversion, Phys. Rev. B **25**, 4515 (1982).
[16] So Takei, Benjamin M. Fregoso, Hoi-Yin Hui, Alejandro M. Lobos, and S. Das Sarma, Soft Superconducting Gap in Semiconductor Majorana Nanowires, Phys. Rev. Lett. **110**, 186803 (2013).
[17] William S. Cole, S. Das Sarma, and Tudor D. Stanescu, Effects of large induced superconducting gap on semiconductor Majorana nanowires, Phys. Rev. B **92**, 174511 (2015).
[18] P. Krogstrup, N. L. B. Ziino, W. Chang, S. M. Albrecht, M. H. Madsen, E. Johnson, J. Nygård, C. M. Marcus, and T. S. Jespersen, Epitaxy of semiconductor-superconductor nanowires, Nat. Mater. **14**, 400 (2015).
[19] W. Chang, S. M. Albrecht, T. S. Jespersen, F. Kuemmeth, P. Krogstrup, J. Nygård, and C. M. Marcus, Hard gap in epitaxial semiconductor-superconductor nanowires, Nat. Nanotechnol. **10**, 232 (2015).
[20] T. Karzig, C. Knapp, R. Lutchyn, P. Bonderson, M. Hastings, C. Nayak, J. Alicea, K. Flensberg, S. Plugge, Y. Oreg, C. Marcus, and M. H. Freedman, Scalable designs for quasiparticle-poisoning-protected topological quantum computation with Majorana zero modes, arXiv:1610.05289.
[21] R. Versluis, S. Poletto, N. Khammassi, N. Haider, D. J. Michalak, A. Bruno, K. Bertels, and L. DiCarlo, Scalable quantum circuit and control for a superconducting surface code, arXiv:1612.08208.
[22] J. Shabani, M. Kjaergaard, H. J. Suominen, Younghyun Kim, F. Nichele, K. Pakrouski, T. Stankevic, R. M. Lutchyn, P. Krogstrup, R. Feidenhans'l, S. Kraemer, C. Nayak, M. Troyer, C. M. Marcus, and C. J. Palmstrøm, Two-dimensional epitaxial superconductor-semiconductor heterostructures: A platform for topological superconducting networks, Phys. Rev. B **93**, 155402 (2016).
[23] M. Kjaergaard, F. Nichele, H. J. Suominen, M. P. Nowak, M. Wimmer, A. R. Akhmerov, J. A. Folk, K. Flensberg, J. Shabani, C. J. Palmstrøm, and C. M. Marcus, Quantized conductance doubling and hard gap in a two-dimensional semiconductor-superconductor heterostructure, Nat. Commun. **7**, 12841 (2016).
[24] M. Hell, M. Leijnse, and K. Flensberg, Two-dimensional platform for networks of Majorana bound states, Phys. Rev. Lett. **118**, 107701 (2017).
[25] F. Pientka, A. Keselman, E. Berg, A. Yacoby, A. Stern, and B. I. Halperin, Topological superconductivity in a planar Josephson junction, arXiv:1609.09482.
[26] B. A. Aminov, A. A. Golubov, and M. Y. Kupriyanov, Quasiparticle current in ballistic constrictions with finite transparencies of interfaces, Phys. Rev. B **53**, 365 (1996).
[27] Christopher R. Reeg and Dmitrii L. Maslov, Hard gap in a normal layer coupled to a superconductor, Phys. Rev. B **94**, 020501 (2016).
[28] A. A. Golubov and M. Y. Kupriyanov, Quasiparticle current in ballistic NcN'S junctions, Physica (Amsterdam) **259C**, 27 (1996).
[29] D. Averin and A. Bardas, ac Josephson Effect in a Single Quantum Channel, Phys. Rev. Lett. **75**, 1831 (1995).
[30] Yong-Joo Doh, Jorden A. van Dam, Aarnoud L. Roest, Erik P. A. M. Bakkers, Leo P. Kouwenhoven, and Silvano De Franceschi, Tunable supercurrent through semiconductor nanowires, Science **309**, 272 (2005).
[31] Jie Xiang, A. Vidan, M. Tinkham, R. M. Westervelt, and Charles M. Lieber, Ge/Si nanowire mesoscopic Josephson junctions, Nat. Nanotechnol. **1**, 208 (2006).
[32] S. Li, N. Kang, D. X. Fan, L. B. Wang, Y. Q. Huang, P. Caroff, and H. Q. Xu, Coherent charge transport in ballistic InSb nanowire Josephson junctions, Sci. Rep. **6**, 24822 (2016).
[33] R. Merservey and B. B. Schwartz, in *Superconductivity*, edited by R. D. Parks (Marcel Dekker Inc., New York, 1969), Vol. 1.
[34] R. Meservey and P. M. Tedrow, Properties of very thin aluminum films, J. Appl. Phys. **42**, 51 (1971).
[35] N. A. Court, A. J. Ferguson, and R. G. Clark, Energy gap measurement of nanostructured aluminium thin films for single Cooper-pair devices, Supercond. Sci. Technol. **21**, 015013 (2008).
[36] M. Octavio, M. Tinkham, G. E. Blonder, and T. Klapwijk, Subharmonic energy-gap structure in superconducting constrictions, Phys. Rev. B **27**, 6739 (1983).
[37] A. W. Kleinsasser, T. N. Jackson, D. McInturff, F. Rammo, G. D. Pettit, and J. M. Woodall, Crossover from tunneling to metallic behavior in superconductor-semiconductor contacts, Appl. Phys. Lett. **57**, 1811 (1990).
[38] J. Nitta, T. Akazaki, H. Takayanagi, and K. Arai, Transport properties in an InAs-inserted-channel In 0.52 Al 0.48 As/In 0.53 Ga 0.47 As heterostructure coupled superconducting junction, Phys. Rev. B **46**, 14286 (1992).
[39] S. N. Artemenko, A. F. Volkov, and A. V. Zaitsev, On the excess current in microbridges S-c-S and S-c-N, Solid State Commun. **30**, 771 (1979).
[40] C. Nguyen, H. Kroemer, and E. L. Hu, Anomalous Andreev Conductance in InAs-AlSb Quantum Well Structures with Nb Electrodes, Phys. Rev. Lett. **69**, 2847 (1992).
[41] C. Nguyen, H. Kroemer, and E. L. Hu, Contact resistance of superconductor-semiconductor interfaces: The case of Nb-InAs/AlSb quantum-well structures, Appl. Phys. Lett. **65**, 103 (1994).
[42] B. Ludoph, N. van der Post, E. N. Bratus, E. V. Bezuglyi, V. S. Shumeiko, G. Wendin, and J. M. van Ruitenbeek, Multiple Andreev reflection in single-atom niobium junctions, Phys. Rev. B **61**, 8561 (2000).
[43] M. T. Allen, O. Shtanko, I. C. Fulga, J. I.-J. Wang, D. Nurgaliev, K. Watanabe, T. Taniguchi, A. R. Akhmerov, P. Jarillo-Herrero, L. S. Levitov, and A. Yacoby, Spatially resolved edge currents and guided-wave electronic states in graphene, Nat. Phys. **12**, 128 (2016).

[44] N. S. Averkiev, L. E. Golub, S. A. Tarasenko, and M. Willander, Theory of magneto-oscillation effects in quasi-two-dimensional semiconductor structures, J. Phys. Condens. Matter **13**, 2517 (2001).

[45] A. F. Volkov, P. H. C. Magnée, B. J. Van Wees, and T. M. Klapwijk, Proximity and Josephson effects in superconductor-two-dimensional electron gas planar junctions, Physica (Amsterdam) **242C**, 261 (1995).

[46] Thomas Schäpers, *Superconductor/Semiconductor Junctions*, Springer Tracts in Modern Physics Vol. 174 (Springer, Berlin, 2001).

[47] L. Casparis, T. W. Larsen, M. S. Olsen, F. Kuemmeth, P. Krogstrup, J. Nygård, K. D. Petersson, and C. M. Marcus, Gatemon Benchmarking and Two-Qubit Operations, Phys. Rev. Lett. **116**, 150505 (2016).